arXiv:2112.01523v2 [cs.CV] 6 Dec 2021

Learning Neural Light Fields with Ray-Space Embedding Networks

Benjamin Attal* Carnegie Mellon University
Jia-Bin Huang Meta
Michael Zollhöfer Reality Labs Research
Johannes Kopf Meta
Changil Kim Meta

https://neural-light-fields.github.io

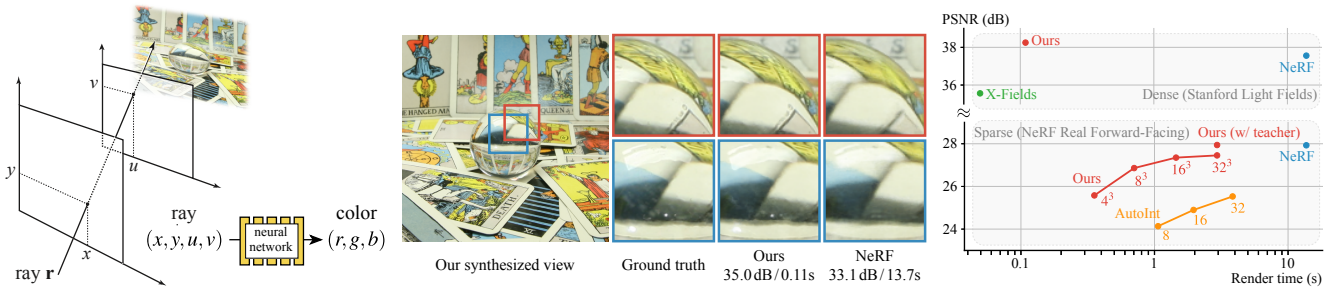

Figure 1. We present *Neural Light Fields with Ray-Space Embedding*, which map rays directly to integrated radiance (*left*). Our representation allows for high-quality view synthesis with faithful reconstruction of complex view dependence (*middle*). We are able to synthesize novel views in a fraction of the time required for the current state-of-the-art approaches, with comparable memory footprint. Our method achieves a more favorable trade-off between quality, speed, and memory than existing approaches for both dense and sparse light fields (*right*).

Abstract

Neural radiance fields (NeRFs) produce state-of-the-art view synthesis results. However, they are slow to render, requiring hundreds of network evaluations per pixel to approximate a volume rendering integral. Baking NeRFs into explicit data structures enables efficient rendering, but results in a large increase in memory footprint and, in many cases, a quality reduction. In this paper, we propose a novel neural light field representation that, in contrast, is compact and directly predicts integrated radiance along rays. Our method supports rendering with a single network evaluation per pixel for small baseline light field datasets and can also be applied to larger baselines with only a few evaluations per pixel. At the core of our approach is a ray-space embedding network that maps the 4D ray-space manifold into an intermediate, interpolable latent space. Our method achieves state-of-the-art quality on dense forward-facing datasets such as the Stanford Light Field dataset. In addition, for forward-facing scenes with sparser inputs we achieve results that are competitive with NeRF-based approaches in terms of quality while providing a better speed/quality/memory trade-off with far fewer network evaluations.

1. Introduction

View synthesis is an important problem in computer vision and graphics. Its goal is to photorealistically render a scene from unobserved camera poses, given a few posed input images. Existing approaches solve this problem by optimizing an underlying functional representation of the scene's appearance and geometry, and then rendering this representation from novel views.

View synthesis has recently experienced a renaissance with an explosion of interest in *neural scene representations* — see Tewari et al. [50,51] for a snapshot of the field. *Neural radiance fields* [30] are perhaps the most popular of these neural representations, and methods utilizing them have recently set the state-of-the-art in rendering quality for view synthesis. A radiance field is a 5D function that maps a 3D point $\mathbf{x}$ and 3D direction $\vec{\omega}$ (with only 2 degrees of freedom) to the radiance leaving $\mathbf{x}$ in direction $\vec{\omega}$, as well as the density of the volume at point $\mathbf{x}$. A neural radiance field or NeRF represents this function with a neural network (usually an MLP). Because volume rendering a NeRF is differentiable, it is straightforward to optimize it by minimizing the difference between the ground truth views at known camera poses and their reconstructions. After optimization, it is simple to predict novel views from a NeRF by employing the same volume rendering procedure.

The main drawback of neural radiance fields is that volume rendering requires many samples and thus many neural

* This work was done while Benjamin was an intern at Meta.

network evaluations per ray to accurately approximate a volume rendering integral. Thus, rendering from a NeRF is usually quite slow. Various approaches exist for baking or caching neural radiance fields into explicit data structures to improve efficiency [11, 15, 38, 62]. However, the storage cost for baked representations is much larger than that of a NeRF, and the baking procedure sometimes leads to a loss in resulting view synthesis quality.

Other methods reduce the number of neural network evaluations per ray by representing radiance only on surfaces [17, 31]. These methods predict new images with only a few evaluations per ray, but suffer from other limitations: Their quality is contingent on good geometry estimates, and they struggle to represent high-frequency view-dependent appearance, as well as volumetric effects and partial transparency.

A *light field* [12, 20] is the integral of a radiance field. It maps ray parameters directly to the integrated radiance along that ray. A common assumption for light fields is that this integral remains the same no matter the ray origin (i.e., radiance is constant along rays), which holds when the convex hull of all camera positions for training and view synthesis does not contain any scene geometry. Given this assumption, a light field is a *function of a ray* on a 4D ray space (Figure 1). Thus, only one look-up of the underlying representation is required to determine the color of a ray, hence one evaluation per pixel unlike hundreds of evaluations required by a NeRF.

In this paper we show how to learn *neural light fields*. Since neural networks have been successfully employed to represent and learn radiance fields from a set of ground truth images, one might think that they could be useful for representing and learning light fields as well. However, we show that learning light fields is significantly harder than learning radiance fields and that using the same neural network architecture as in NeRF to parameterize a light field leads to issues in terms of training stability and interpolation quality for view synthesis. We argue that NeRF alleviates these challenges with two clever design choices: 1) While a radiance field is a 5D function, the domain of a NeRF is close to a 3D manifold due to the fact that its network is early-conditioned by 3D position and late-conditioned by 2D viewing direction [30]; 2) It learns the scene geometry as a density field in 3D space, which makes a NeRF effectively a 3D geometric representation and guarantees multi-view consistency when new views are rendered.

On the other hand, we face the problem of learning a function defined on a 4D ray space from only partial observations — input images only cover a few 2D slices of the full 4D space, while NeRF enjoys multiple observations of most 3D points within their near-3D domain. Further, light fields themselves do not entail any form of scene geometry, which poses significant challenges in interpolating unseen rays in a geometrically meaningful way. Existing methods address these issues by sacrificing view interpolation [8], leveraging data driven priors [46], or relying on strong supervision signals [22].

In order to deal with these challenges, we employ a set of instruments: a novel ray-space embedding approach, spatial subdivision, and soft student-teacher regularization. The *ray-space embedding network* re-maps the input ray-space into an embedded latent space that facilitates both the registration of rays observing same 3D points and the interpolation of unobserved rays, which allows for both better memorization and view synthesis. While the embedding network alone already provides state-of-the-art view synthesis quality for densely sampled inputs (such as the Stanford light fields [56]), it does not handle long-range correspondences between rays in sparser input sequences (such as those from the Local Light Field Fusion dataset [29]).

To mitigate these issues, we learn a voxel grid of *local light fields*, where each local light field is less prone to complex occlusions and texture changes. Therefore, each local light field has to learn a simpler embedding at the price of several more network evaluations (one for each intersected subdivision) per ray. Finally, we provide an optional way to bootstrap the training process using a NeRF as a *teacher* signal. Unlike the existing methods [22], our learned representation is not capped by the teacher signal, and achieves higher quality view synthesis than the teacher.

We evaluate our method for learning neural light fields in both sparse and dense regimes. We compare to state-of-the-art view-synthesis methods, and show that our approach achieves better view synthesis quality in both regimes, in a fraction of render time that other methods require, while still maintaining their small memory footprint (Figure 1).

In summary, our contributions are:

1. A novel neural light field representation that employs a ray-space embedding network and achieves state-of-the-art quality for small-baseline view synthesis without any geometric constraints.
2. A subdivided neural light field representation for large baseline light fields that leads to a good trade-off in terms of the number of evaluations vs. quality, which can be optimized to outperform NeRF for real-world scenes.

2. Related Work

Light Fields. Light fields [20] or Lumigraphs [12] represent the flow of light at all positions in 3D space, in all viewing directions. By resampling the rays from the discrete set of captured images, one can synthesize photorealistic novel views of a static scene without necessitating geometric reconstruction. However, this often involves capturing and storing an excessive number of images. Much effort has been devoted to extending light fields to unstructured input cameras [4, 7] and synthesizing (i.e. interpolating) in-

between views for light fields [16, 42, 55, 58, 59, 61]. Very recently, neural implicit representations have been applied to modeling light fields for better compactness [8] and for faster rendering for view synthesis [22, 46]. Our work leverages *neural* light fields as its core representation for view synthesis. Unlike prior work [8] in neural light fields that aims to represent and memorize the radiance of *observed* rays only, our focus is to synthesize the radiance of *unseen/novel* rays for view synthesis. Additionally, our approach is capable of capturing and reproducing challenging view-dependent effects in real scenes. Our method is similar to AutoInt [22], which predicts integrated radiance along rays and uses subdivision. The accuracy of AutoInt, however, is lower than NeRF due to the approximation of the nested volume integral. By contrast, our approach leads to improved performance over NeRF.

Representations for View Synthesis. Various 3D representations have been developed for rendering novel views from a sparse set of captured images. Image-based rendering techniques leverage proxy geometry (often in the form of a mesh or per-frame depth maps) to warp and blend source image content into novel views [4, 6, 36, 44]. Recent advances in image-based rendering include learning-based disparity estimation [9, 16], blending [14, 39], and image synthesis via 2D CNNs [39, 40]. Other commonly used scene representations include voxels [25, 47], 3D point clouds [1, 18, 41] or camera-centric layered 3D representations, such as multi-plane images [3, 29, 53, 57, 64] or layered depth images [13, 19, 43, 54]. Rather than using discrete representations as in the above methods, a recent line of work explores neural representations to encode the scene geometry and appearance as a continuous volumetric field [2, 23, 27, 30, 48]. We refer the readers to [50] for more comprehensive discussions of these works. Many of these methods learn a mapping from *3D points* (and 2D viewing directions) to color/density, which can be rendered using volume integration – thus, rendering the color of a pixel for novel views often requires hundreds of MLP evaluations. Instead, our approach directly learns the mapping from *a single ray* to color, and therefore supports efficient rendering without requiring postprocessing/baking.

Coordinate-based Representations. Coordinate-based representations have emerged as a powerful tool for overcoming the limitations of traditional discrete representations (e.g., images, meshes, voxelized volumes). The core idea is to train an MLP to map an input coordinate to the desired target value such as pixel color [26, 32, 45, 60], signed distance [5, 33], occupancy [28], volume density [30], or semantic labels [63]. Like existing coordinate-based representation approaches, our method also learns the mapping from an input coordinate (ray) to a target scene property (color). Our core contributions lie in designing a coordinate embedding network which enables plausible view synthesis from a sparse set of source images.

Learned Coordinate Embedding. Learned coordinate transformation or embedding has been applied to extend the capability of coordinate-based representations, such as NeRF, for handling higher dimensional interpolation problems. For example, several works tackle dynamic scene view synthesis [10, 21, 34, 52] by mapping space at each time-step into a canonical frame. Others leverage coordinate embedding for modeling articulated objects such as the human body [24, 35]. Our ray-space embedding network can be viewed as *locally deforming* the input ray coordinates such that the MLP can produce plausible view interpolation while preserving faithful reconstruction of the source views.

Subdivision. Recent coordinate-based representations employ 3D space partitioning/subdivision either for improving the rendering efficiency [15, 38, 62] or representation accuracy [26, 37]. Our work also leverages spatial subdivision and in doing so shows improved rendering quality, particularly on scenes with large camera baselines.

3. Neural Light Fields

A neural radiance field [30] represents the appearance and geometry of a scene with an MLP $F_{\boldsymbol{\theta}} : (\mathbf{x}_t, \vec{\boldsymbol{\omega}}) \rightarrow (L_{\mathrm{e}}(\mathbf{x}_t, \vec{\boldsymbol{\omega}}), \sigma(\mathbf{x}_t))$ with trainable weights $\boldsymbol{\theta}$. It takes as input a 3D position $\mathbf{x}_t$ and a viewing direction $\vec{\boldsymbol{\omega}}$, and produces both the density $\sigma(\mathbf{x}_t)$ at point $\mathbf{x}_t$ and the radiance $L_{\mathrm{e}}(\mathbf{x}_t, \vec{\boldsymbol{\omega}})$ emitted at point $\mathbf{x}_t$ in direction $\vec{\boldsymbol{\omega}}$.

We can generate views of the scene from this MLP using volume rendering:

$$L(\mathbf{x}, \vec{\boldsymbol{\omega}}) = \int_{t_{\mathrm{n}}}^{t_{\mathrm{f}}} \underbrace{T(\mathbf{x}, \mathbf{x}_t)}_{\text{Acc. transmittance}} \underbrace{\sigma(\mathbf{x}_t)}_{\text{Density}} \underbrace{L_{\mathrm{e}}(\mathbf{x}_t, \vec{\boldsymbol{\omega}})}_{\text{Emitted radiance}} \, \mathrm{d}t, \qquad (1)$$

where $T(\mathbf{x}, \mathbf{x}_t) = e^{-\int_{t_n}^{t} \sigma(\mathbf{x}_s)\,\mathrm{d}s}$ describes the accumulated transmittance for light propagating from position $\mathbf{x}$ to $\mathbf{x}_t$, for near and far bounds $t \in [t_{\mathrm{n}}, t_{\mathrm{f}}]$ of the scene. In practice, we approximate the integral using numerical quadrature:

$$L(\mathbf{x}, \vec{\boldsymbol{\omega}}) \approx \sum_{k=1}^{N} \hat{T}(\mathbf{x}, \mathbf{x}_k)\,(1 - e^{-\sigma(\mathbf{x}_k)\Delta\mathbf{x}_k})\,L_{\mathrm{e}}(\mathbf{x}_k, \vec{\boldsymbol{\omega}}), \qquad (2)$$

where $\hat{T}(\mathbf{x}, \mathbf{x}_k) = e^{-\sum_{j=1}^{k} \sigma(\mathbf{x}_j)\Delta\mathbf{x}_j}$ and $\Delta\mathbf{x}_j = \mathbf{x}_j - \mathbf{x}_{j-1}$ is the distance between adjacent samples. An accurate approximation of (1) requires many samples and thus many neural network evaluations (on the order of hundreds) per ray.

Light Fields. Whereas a radiance field represents the radiance emitted at each point in space, a light field represents the total *integrated radiance* traveling along a ray. In other words, Equations (1) and (2) describe the relationship between the light field L and the radiance field (L_e, σ). By optimizing a *neural light field* representation for L, given an input ray, one can predict this integrated radiance (and

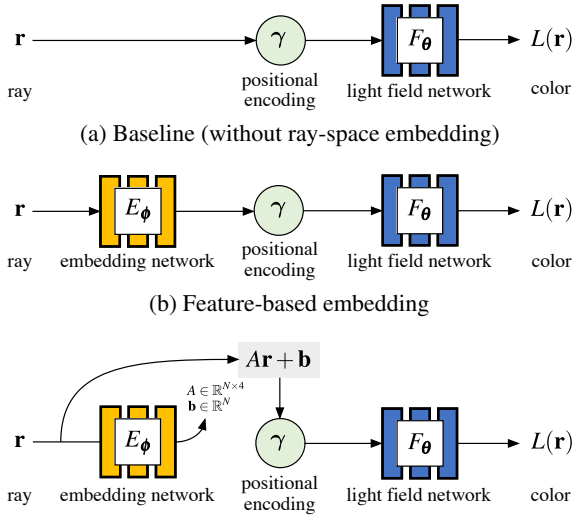

Figure 2. **Ray-space embedding networks**. Building upon the baseline (a), we explore two different schemes for ray-space embedding: (b) predicting the latent features and (c) predicting affine transformation parameters.

therefore render the color along this ray) with only a single neural network evaluation.

Assuming that we are operating on forward facing scenes, and that radiance remains constant along rays, we can construct a 4D ray space by intersecting rays with two planes, π^{xy} and π^{uv}. We can then take the local planar coordinates, $(x,y) \in \pi^{xy}$ and $(u,v) \in \pi^{uv}$ of these ray intersections as the ray parameterization for the 4D light field, $L : \mathbf{r} = (x,y,u,v) \rightarrow \mathbf{c} = (r,g,b)$; see Figure 1(*left*).

Baseline Neural Light Fields. Similar to how NeRF uses an MLP to represent radiance fields, we define an MLP $F_{\boldsymbol{\theta}}$ to represent a light field. It takes as input positionally encoded 4D ray coordinates $\boldsymbol{\gamma}(\mathbf{r})$ and outputs color $\mathbf{c}$ (integrated radiance) along each ray (Figure 2a):

$$L_{\text{base}}(\mathbf{r}) = F_{\boldsymbol{\theta}}(\boldsymbol{\gamma}(\mathbf{r}))\,. \tag{3}$$

This baseline approach, however, is an unsatisfactory light field representation due to the following challenges. First, the captured input images only provide *partial observations* in the form of a sparse set of 2D slices of the full 4D ray space, so that each 4D ray coordinate in the input training data is observed at most once. Because of this, the network will require many more training iterations to "memorize" the input. Second, light fields do not explicitly represent 3D scene geometry; hence the network a priori does not know how to *interpolate* the colors of unobserved rays from training observations. In other words, when querying a neural network representing a light field with *unseen* ray coordinates, multi-view consistency is not guaranteed. To address these challenges, we present three key techniques — ray-space embedding, subdivision, and student-teacher regularization — which substantially improve the rendering quality of the proposed neural light field representation.

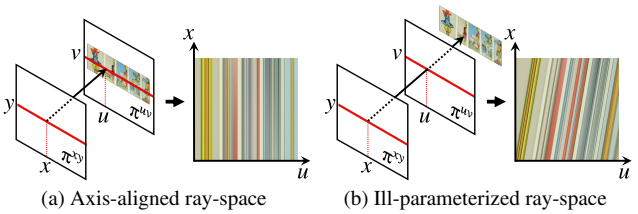

Figure 3. **Importance of light field parameterization**. (a) It is easy to learn a light field for a well-parameterized ray-space, but (b) a ray-space with non-axis-aligned level sets makes the problem more challenging, especially when using Fourier features [49].

4. Ray-Space Embedding Networks

We introduce *ray-space embedding networks*. This network re-maps the input ray-space into an *embedded latent space*. Intuitively, our goals for ray-space embedding networks are:

1. **Memorization:** Map disparate coordinates in input 4D ray-space that observe the same 3D point to the same location in the latent space. This allows for more stable training and better allocation of network capacity, and thus better memorization of input views.
2. **Interpolation:** Produce an interpolable latent space, such that querying unobserved rays preserves multi-view consistency and improves view synthesis quality.

Feature-Space Embedding. A straightforward approach would be to learn a nonlinear mapping from 4D ray coordinates to a latent feature space via an MLP, $E_{\boldsymbol{\phi}}^{\text{feat}} : \mathbf{r} \rightarrow \mathbf{f} \in \mathbb{R}^N$, where N is the feature space dimension (see Figure 2b). This embedding network can produce a nonlinear, many-to-one mapping from distinct ray coordinates into shared latent features, which would allow for better allocation of capacity to the downstream light field network $F_{\boldsymbol{\theta}}$. The finite capacity of $F_{\boldsymbol{\theta}}$ incentivizes this "compression" and thus encourages rays with similar colors to be mapped to nearby features in the latent space; effectively a form of implicit triangulation.

After embedding, we then feed the positionally encoded N-dimensional feature into the light field MLP $F_{\boldsymbol{\theta}}$:

$$L_{\text{feat}}(\mathbf{r}) = F_{\boldsymbol{\theta}}(\boldsymbol{\gamma}(E_{\boldsymbol{\phi}}^{\text{feat}}(\mathbf{r})))\,. \tag{4}$$

While this approach compresses and helps to find correspondences in ray space, it is not enough to facilitate the interpolation between these correspondences (see Section 6).

Neural Light Field Re-parameterization. To understand our goals better, consider a scene containing an axis-aligned textured square at a fixed z-depth. Again, we assume a two-plane parameterization for the input ray-space of this scene. If one of the planes is at the depth of the square, then the light field will only vary in two coordinates, as illustrated in Figure 3a. In other words, the light field is only a function

of (u,v) and is constant in (x,y). Since positional encoding is applied separately for each input coordinate, the baseline model (3) can interpolate the light field perfectly if it chooses to ignore the positionally encoded coordinates (x,y).

On the other hand, if the two planes in the parameterization do not align with the textured square, the color level sets of the light field are 2D affine subspaces, denoted by $g(s,t)$, that are *not* axis-aligned (see Figure 3b). Intuitively, the positional encoding of g will vary in a highly non-linear way along the 2D s-t parameter space, producing a much more complex level set than in the axis-aligned case. It is then more difficult, and requires more network capacity, to learn to map $\gamma(g(s,t))$ to a single color. See the appendix for a more extensive discussion.

One can therefore frame the task of effective interpolation as learning an optimal *re-parameterization* of the light field, such that the 2D color level sets for each 3D scene point are axis-aligned. Assuming that the re-parameterization is locally smooth (ideally constant along the 2D affine subspace corresponding to a 3D point), it will enable good interpolation (see Figure 7).

Local Affine-Transformation Embedding. Given this intuition, we describe our architecture for ray-space embedding, which learns *local affine transformations* for each coordinate in ray space. We learn local affine transformations rather than a single global transformation because different rays may correspond to points with different depths, which will cause the color level sets at these locations to vary.

To this end, we employ an MLP $E_\phi : \mathbf{r} \rightarrow (A \in \mathbb{R}^{N\times 4}, \mathbf{b} \in \mathbb{R}^N)$. The output of the network is a $N \times 4$ matrix A, as well as an N-vector $\mathbf{b}$ representing a bias (translation), which together form a 4D$\rightarrow N$D affine transformation. This affine transformation is applied to the input ray coordinate $\mathbf{r}$ before being positionally encoded and passed into the light field network F_θ:

$$L(\mathbf{r}) = F_\theta(\gamma(A\mathbf{r}+\mathbf{b})), \text{ where } (A,\mathbf{b}) = E_\phi(\mathbf{r}). \quad (5)$$

See Figure 2c for an illustration of this model.

5. Subdivided Neural Light Fields

When training data samples the input ray-space too sparsely, our embedding network struggles to find long-range correspondences between training rays. Moreover, even if it can discover correspondences, interpolation for unobserved rays in between these correspondences remains underconstrained.

To resolve these issues, we propose learning a voxel grid of *local* light fields. This approach is motivated by the following observation: if we parameterize a local light field for a voxel by intersecting rays with the voxel's front and back planes, the color level sets of the local light field are already *almost axis-aligned*. As such, the ray-space embedding for each voxel can be simple, only inducing small shears of the input ray-space in order to allow for good interpolation. On the other hand, a global light field requires learning a complex ray-space embedding that captures occlusions and large depth changes.

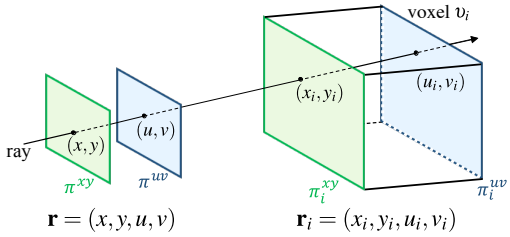

Figure 4. **Re-parameterization for local light fields**. A ray $\mathbf{r} = (x,y,u,v)$ defined globally is re-parameterized with respect to each local light field in voxel v_i, by intersecting the front and back faces of v_i. This yields local ray coordinates $\mathbf{r}_i = (x_i, y_i, u_i, v_i)$.

Therefore a local light field can be learned much more easily than a full global light field *with the same training data*. This still requires that we solve an assignment problem: we must know which rays to use to train each local light field. While we can easily exclude all rays that do not intersect the voxel containing the local light field, still many other rays may be occluded by other geometry before they hit the voxel. These rays should also be excluded during training.

A simple way to handle ray-assignment is by learning opacity. If the opacity accumulated along a ray before it hits a voxel is high, this ray should receive little contribution from this voxel, and contributes little to this voxel's gradient during training; and similarly, if the opacity accumulated along a ray *within* the voxel is small. Therefore, we modify our (local) light field network to also produce *integrated* opacity, or alpha.

Subdivided Volume Rendering. We detail how a set local light fields represent a scene and how they can be rendered to form new images. Given a voxel grid in 3D space, the light field within each voxel is parameterized with respect to the voxel's front and back planes (See Figure 4), yielding the ray coordinates $\mathbf{r}_i$, where i is some voxel index, for any ray $\mathbf{r}$ defined globally. If the 3D space is subdivided into M voxels, there exist M distinct but equivalent parameterizations $\{\mathbf{r}_i\}_{i=1}^M$ of each ray $\mathbf{r}$.

To implement this model, the embedding network E_ϕ is augmented such that it takes the positionally encoded voxel index $\gamma(i)$ in addition to the 4D ray coordinates, i.e., $E_\phi : (\mathbf{r}_i, \gamma(i)) \rightarrow (A_i, \mathbf{b}_i)$. The light field network F_θ is augmented in the same way, and also predicts both color *and* alpha: $F_\theta : (\gamma(A_i\mathbf{r}_i + \mathbf{b}_i), \gamma(i)) \rightarrow (\mathbf{c}_i, \alpha_i)$, where α_i is *integrated* opacity within the voxel v_i, just as $\mathbf{c}_i$ is the integrated radiance therein.

Given this model, rendering works in the following way. First, the set of voxels $\mathcal{V}(\mathbf{r})$ that the ray $\mathbf{r}$ intersects are identified. The ray is then intersected with the voxel's front and back planes π_i^{xy} and π_i^{uv}. This process yields a series of

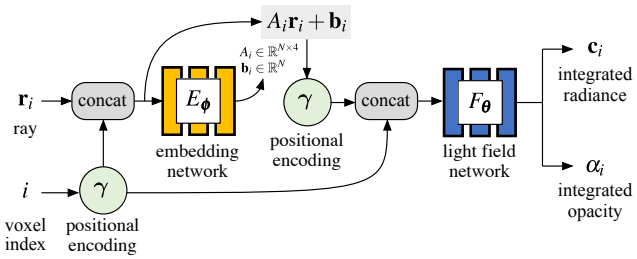

Figure 5. **Local light fields via spatial subdivision**. Each local light field takes a locally re-parameterized ray $\mathbf{r}_i$ and its voxel index i and predicts both the radiance and opacity integrated for the ray segment traveling through the voxel. Both the embedding network E_ϕ and the light field network F_θ are conditioned on positionally encoded voxel index $\gamma(i)$.

local ray coordinates $\{\mathbf{r}_i\}_{v_i\in\mathcal{V}(\mathbf{r})}$. The color $\mathbf{c}_i$ and alpha α_i of each $\mathbf{r}_i$ are then computed as:

$$(\mathbf{c}_i, \alpha_i) = F_\theta(\gamma(A_i\mathbf{r}_i + \mathbf{b}_i), \gamma(i)), \tag{6}$$

where the local affine-transformation is obtained from the embedding network:

$$(A_i, \mathbf{b}_i) = E_\phi(\mathbf{r}_i, \gamma(i)). \tag{7}$$

The final color of ray $\mathbf{r}$ is then over-composited from back to front:

$$\mathbf{c} = \sum_{i\in\mathcal{V}(\mathbf{r})} \Big(\prod_{j\in\mathcal{V}(\mathbf{r})\wedge j<i} (1-\alpha_j) \Big) \alpha_i \mathbf{c}_i, \tag{8}$$

which assumes the voxel indices are sorted by the distances from the ray origin in descending order (see Figure 5).

6. Experiments

Datasets. We evaluate our model in two angular sampling regimes: sparse (wide-baseline) and dense (narrow-baseline), using the Real Forward-Facing dataset [30] and the Stanford Light Field dataset [56], respectively. Each scene from the Real Forward-Facing dataset consists of a few dozen images and exhibits relatively large angular separation in between views. We followed the authors' train/test split and hold out every 8th image from training. The Stanford light fields are all captured as 17×17 dense 2D grids of images. We hold out every 4th image in *both* horizontal and vertical directions and use the resulting 5×5 subsampled light field for training, while reserving the rest of the images for testing. We downsample the images in the Real Forward-Facing dataset by a factor of 8, and use half of the original resolution of the Stanford scenes in all our experiments. For quantitative metrics, we report PSNR, SSIM, LPIPS, and FPS; where FPS is computed for 512×512 pixel images.

Baseline Methods. We compare our model with NeRF [30] and AutoInt [22] (with 32 sections) on the sparse dataset. NeRF is a state-of-the-art view synthesis method, while AutoInt learns integrated radiance and employs subdivision, similar to our approach. We did not include the following methods, although they are related, for various reasons: PlenOctrees [62], KiloNeRF [38], and NSVF [23] operate on bounded 360-degree scenes only; SNeRG [15] strictly underperforms NeRF on the Real Forward-Facing dataset. On the dense dataset (Stanford), we compare our model to NeRF and X-Fields [2], which is a state of the art in light field interpolation. Kalantari et al. [16] would also be a relevant comparison, but X-Fields outperforms it, hence we did not include it in our evaluations.

Table 1. **Quantitative comparisons.** On both sparse (Real Forward-Facing [30]) and dense (Stanford [56]) light fields. We show the aggregated metrics over all scenes in each dataset.

Dataset	Method	PSNR↑	SSIM↑	LPIPS↓	FPS↑
Sparse	NeRF [30]	27.928	0.9160	0.065	0.07
	AutoInt [22] (32 sections)	25.531	0.853	0.156	0.26
	Ours (32^3 grid)	27.454	0.905	**0.060**	**0.34**
	Ours (32^3 grid; w/ teacher)	**27.941**	**0.9161**	0.068	
Dense	NeRF [30]	37.559	0.979	0.037	0.07
	X-Fields [2]	35.559	0.976	0.036	**20.0**
	Ours	**38.054**	**0.982**	**0.020**	9.14

Implementation Details. For our feature-based embedding (4), we set the embedding space dimension to $N = 32$. The embedded feature $\mathbf{f}$ is ℓ_2-normalized and then multiplied by $\sqrt{32}$, such that on average, each output feature has a square value close to one. For our local affine transformation–based embedding (5), we infer 32×4 matrices and 32D bias vectors, so the embedding dimension is still 32. We then normalize the matrices A with their Frobenius norm and multiply them by $\sqrt{32\cdot 4}$. We use a *tanh*-activation for our predicted bias vectors.

For positional encoding $\gamma(\cdot)$ we use $L = 8$ frequency bands for our subdivided model and $L = 10$ frequency bands for our one-evaluation model. Higher frequencies are gradually eased in using windowed positional encoding, following Park et al. [34], over 50k iterations with subdivision, or 80k without. For both models we use a 8-layer, 256 hidden unit MLP with one skip connection for E_ϕ and an 8-layer 256 hidden unit MLP with one skip connection for F_θ. Note that we still share a single network each for E_ϕ and F_θ for all local light fields in our subdivided model, which are indexed with the voxel center points $\mathbf{p}_i$, i.e., $i \equiv \mathbf{p}_i$. We use a batch size of 4,096 for our subdivided model, and a batch size of 8,192 for our one-evaluation model during training and run all experiments on a single Tesla V100 GPU with 16 GB of memory. Please refer to the appendix and our project webpage for further details and results. We will release the source code and pre-trained models to facilitate future research.

Soft Student-Teacher Regularization. We optionally regularize our model with additional *teacher* signals using

Figure 6. **Visual comparisons.** We show our view synthesis results of several Real Forward-Facing and Stanford scenes in the leftmost column. The close-ups reveal our representation leads to more faithful reconstruction of view dependent effects (*Horns*, *T-Rex*, and *Treasure*) and sharper results (*Flower* and *Flowers*). See our *supplementary material* for more results.

trained NeRFs, which helps bootstrap the training process. We ease out this additional signal gradually. Specifically, we render a 10×10 grid of images from a trained NeRF and include these images in our training set. Teacher influence is gradually decreased throughout training by decaying the loss for the predicted images by a factor of 0.25 every 500 epochs. This leads to improved multi-view consistency and better numerical performance than the teacher (Table 1), with slightly worse reproduction of view dependence than our model without regularization (Figure 6).

Quantitative Evaluation. Table 1 compares view synthesis quality using the metrics aggregated over held out images in all scenes. For the Real Forward-Facing data (upper half), we used 32^3 subdivision with and without teacher signals. We cite the AutoInt results with 32 sections, which provide a comparable render-time trade-off to our subdivision. Without teacher, our method outperforms AutoInt in both quality ($\sim$2 dB) and speed ($\sim$30%) while performing competitively with NeRF on PSNR and SSIM (within 0.5 dB in quality) and rendering more than $\times$4.5 times faster. Additionally, we outperform NeRF on the LPIPS metrics. With teacher regularization, ours outperforms NeRF on both PSNR and SSIM, while suffering slightly on LPIPS. It takes about 20 hours to train our model at 32^3 resolution without regularization, and 26 hours to train our model with regularization. NeRF takes approximately 18 hours to train.

For the Stanford data, we train our model for about 10 hours. For baseline comparisons, we double the default capacity of the X-Fields model as well as the number of images used for interpolation; and train X-Fields for 8 hours rather than the maximum time of 172 minutes listed in their paper [2]. Our method outperforms both NeRF and X-Fields in all three metrics. Specifically, our model performs better on more complex scenes, e.g., "Treasure" and "Bulldozer", with complicated geometry and high-frequency textures, while NeRF performs slightly better on simpler scenes like "Chess" and "Beans". Our model renders a frame in about 0.11 seconds in this setup. See our project webpage for more details.

Reconstruction of View Dependence. Our approach reconstructs view dependence better than the baseline methods (see Figure 1(*middle*) and 6). This is especially prominent with high-frequency view-dependent effects such as reflection and refraction.

Memory Footprint. Table 2 shows the model sizes. Our model has a similar memory footprint to NeRF. Training time depends on the number of subdivisions employed, with faster training times than NeRF for no or few subdivisions, and comparable training times for more subdivisions. Overall, our method provides the best trade-off between quality, rendering speed, and memory among the baselines we compared to; see the graphs in Figure 1(*right*).

Ablations on Embedding Networks. We study the effect of our proposed embedding networks via ablations. See Table 3 for quantitative evaluation with varying configurations. With no embedding and only positional encoding (baseline),

Table 2. **Memory footprint** of our model compared to other methods in terms of the number of trainable weights in each network. For X-Fields [2] we include the memory footprint of the model, and of the training images which must be maintained in order to synthesize novel views.

Method	Ours	NeRF [30]	AutoInt [22]	X-Fields [2]
Size (MB)	5.4	4.6	4.6	3.8 / 75

Table 3. **Ablations on the ray-embedding network.** On both sparse (Real Forward-Facing [30]) and dense (Stanford [56]) light fields. Student-teacher training was *not* used.

Dataset	Method	Embedding	PSNR↑	SSIM↑	LPIPS↓
Sparse	Ours (32^3 grid)	Not used (3)	26.696	0.888	0.079
		Feature (4)	26.922	0.891	0.073
		Local affine (5)	27.454	0.905	**0.060**
	NeRF [30]		**27.928**	**0.916**	0.065
Dense	Ours	Not used (3)	25.111	0.841	0.098
		Feature (4)	37.120	0.9792	0.030
		Local affine (5)	**38.054**	**0.982**	**0.020**
	NeRF [30]		37.559	0.9790	0.037

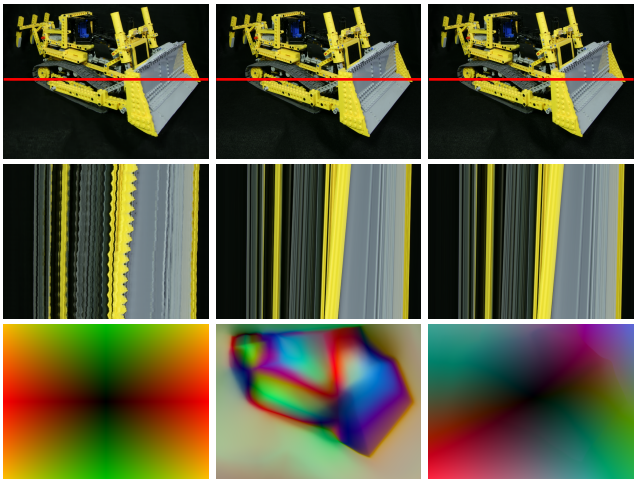

Figure 7. **Effect of different embeddings**. The *top* row shows predicted images, *middle* predicted EPIs, and *bottom* a visualization of the embedding space for each method. The model without an embedding network (*left*) predicts images with distortions, and interpolates poorly. The feature embedding network (*center*) learns a salient latent space that registers disparate rays. It interpolates views fairly well, but color level sets corresponding to a point are not always planar, which leads to decreased overall quality. The local affine transformation embedding (*right*) learns a smooth set of affine transformations, yielding an embedding space that enables both high quality prediction and good interpolation. Difference in quality between feature and local affine embedding is far more obvious in video comparisons. See our supplemental material.

the network does not produce multi-view consistent view synthesis and the output exhibits severe wobbling artifacts with distorted EPI level curves (see Figure 7).

The use of our feature-based embedding leads to a boost in quality over the baseline. In particular, it achieves our first objective of embedding ("memorization"). Indeed, the embedding network finds correspondences between input ray-space coordinates that observe the same scene points. However, it can still struggle to interpolate these correspondences appropriately in between views, i.e., while identifying rays mapping to the same point, it does not necessarily know which intermediate unobserved rays map to that same point.

Our local affine transformation embedding allows the network to achieve better interpolation quality. Because the embedding network that predicts affine transformations does not use positional encoding, the predicted transformations vary smoothly. Thus, level sets in the embedding space are already close to locally planar, and we learn a model that interpolates in a (locally) view consistent way for free. We believe it would be interesting to look at transforms that predict more expressive level sets for different kinds of view dependence, or perhaps learn a model for these transforms from a large collection of light field data, which we leave as future work.

Table 4. **Ablations on the subdivision.** On sparse light fields (Real Forward-Facing [30]) only. Student-teacher training was *not* used.

Method	Subdivision	PSNR↑	SSIM↑	LPIPS↓	FPS↑
Ours	4^3 grid	25.579	0.867	0.094	**2.82**
	8^3 grid	26.860	0.893	0.070	1.42
	16^3 grid	27.350	0.904	0.062	0.69
	32^3 grid	27.454	0.905	**0.060**	0.34
AutoInt [22]	8 sections	24.136	0.820	0.176	0.94
	16 sections	24.898	0.836	0.167	0.51
	32 sections	25.531	0.853	0.156	0.26
NeRF [30]		**27.928**	**0.916**	0.065	0.07

Ablations on Subdivision. Table 4 and Figure 1(*right*) summarize the trade-off between the quality and rendering speed of our model on various resolutions of spatial subdivision, compared to NeRF and AutoInt. As expected, our model archives better quality view synthesis as we employ more local light fields with finer spatial subdivision, trading off the rendering speed. The render-time increases linearly to the number of subdivided voxels along the ray direction. Our method provides better quality and speed than AutoInt at all comparable subdivision levels.

Limitations. We focus on light fields parameterized with two planes. Although common, this does not encompass 360° scenes, for example. While spherical and Plücker coordinates [46] can be used, we believe additional considerations would be necessary in the design of embedding networks for such scenes. Our training scheme requires additional geometry-motivated regularization for sparse light fields: subdivision and teacher signals. They come at the cost of both increased render time and training time. Additionally, using a teacher such as NeRF leads to slightly worse reproduction of view dependence (Figure 6). Other regularization schemes, including those that do not require pre-training a teacher, should be investigated further. The insights obtained from our approach could potentially be integrated into the design of embedding networks. In particular, certain priors for embedding could be learned from data. Finally, adaptive subdivision [23, 26] is an interesting direction for future work which could lead to better quality without sacrificing speed.

7. Conclusion

We present *neural light fields* and propose novel ray-space embedding networks for learning them. To deal with sparse input, we introduce subdivision and regularization schemes. Our representation enables state-of-the-art rendering quality in a fraction of the render time that many existing methods require, and achieves a better trade-off between quality, speed, and memory. We believe our method can open up new avenues for view synthesis, and that it has implications for other high-dimensional interpolation problems such as view-time or view-time-illumination interpolation [2].

References

[1] Kara-Ali Aliev, Artem Sevastopolsky, Maria Kolos, Dmitry Ulyanov, and Victor Lempitsky. Neural point-based graphics. In *ECCV*, 2020. 3

[2] Mojtaba Bemana, Karol Myszkowski, Hans-Peter Seidel, and Tobias Ritschel. X-fields: implicit neural view-, light- and time-image interpolation. *ACM Trans. Graph.*, 39(6):257:1–257:15, 2020. 3, 6, 7, 8, 13

[3] Michael Broxton, John Flynn, Ryan Overbeck, Daniel Erickson, Peter Hedman, Matthew Duvall, Jason Dourgarian, Jay Busch, Matt Whalen, and Paul Debevec. Immersive light field video with a layered mesh representation. *ACM Transactions on Graphics (TOG)*, 39(4):86–1, 2020. 3

[4] Chris Buehler, Michael Bosse, Leonard McMillan, Steven Gortler, and Michael Cohen. Unstructured lumigraph rendering. In *Proceedings of the 28th annual conference on Computer graphics and interactive techniques*, 2001. 2, 3

[5] Rohan Chabra, Jan E Lenssen, Eddy Ilg, Tanner Schmidt, Julian Straub, Steven Lovegrove, and Richard Newcombe. Deep local shapes: Learning local sdf priors for detailed 3d reconstruction. In *ECCV*, 2020. 3

[6] Gaurav Chaurasia, Sylvain Duchene, Olga Sorkine-Hornung, and George Drettakis. Depth synthesis and local warps for plausible image-based navigation. *ACM Transactions on Graphics (TOG)*, 32(3):1–12, 2013. 3

[7] Abe Davis, Marc Levoy, and Fredo Durand. Unstructured light fields. In *Eurographics*, 2012. 2

[8] Brandon Yushan Feng and Amitabh Varshney. Signet: Efficient neural representation for light fields. In *ICCV*, 2021. 2, 3

[9] John Flynn, Ivan Neulander, James Philbin, and Noah Snavely. Deepstereo: Learning to predict new views from the world's imagery. In *CVPR*, 2016. 3

[10] Chen Gao, Ayush Saraf, Johannes Kopf, and Jia-Bin Huang. Dynamic view synthesis from dynamic monocular video. In *ICCV*, 2021. 3

[11] Stephan J. Garbin, Marek Kowalski, Matthew Johnson, Jamie Shotton, and Julien Valentin. Fastnerf: High-fidelity neural rendering at 200fps. In *ICCV*, 2021. 2

[12] Steven J Gortler, Radek Grzeszczuk, Richard Szeliski, and Michael F Cohen. The lumigraph. In *Proceedings of the 23rd annual conference on Computer graphics and interactive techniques*, 1996. 2

[13] Peter Hedman, Suhib Alsisan, Richard Szeliski, and Johannes Kopf. Casual 3d photography. *ACM Transactions on Graphics (TOG)*, 36(6):1–15, 2017. 3

[14] Peter Hedman, Julien Philip, True Price, Jan-Michael Frahm, George Drettakis, and Gabriel Brostow. Deep blending for free-viewpoint image-based rendering. *ACM Transactions on Graphics (TOG)*, 37(6):1–15, 2018. 3

[15] Peter Hedman, Pratul P Srinivasan, Ben Mildenhall, Jonathan T Barron, and Paul Debevec. Baking neural radiance fields for real-time view synthesis. *ICCV*, 2021. 2, 3, 6

[16] Nima Khademi Kalantari, Ting-Chun Wang, and Ravi Ramamoorthi. Learning-based view synthesis for light field cameras. *ACM Transactions on Graphics (TOG)*, 35(6):1–10, 2016. 3, 6

[17] Petr Kellnhofer, Lars Jebe, Andrew Jones, Ryan Spicer, Kari Pulli, and Gordon Wetzstein. Neural lumigraph rendering. In *CVPR*, 2021. 2

[18] Georgios Kopanas, Julien Philip, Thomas Leimkühler, and George Drettakis. Point-based neural rendering with per-view optimization. *Computer Graphics Forum*, 40(4):29–43, 2021. 3

[19] Johannes Kopf, Kevin Matzen, Suhib Alsisan, Ocean Quigley, Francis Ge, Yangming Chong, Josh Patterson, Jan-Michael Frahm, Shu Wu, Matthew Yu, et al. One shot 3d photography. *ACM Transactions on Graphics (TOG)*, 39(4):76–1, 2020. 3

[20] Marc Levoy and Pat Hanrahan. Light field rendering. In *Proceedings of the 23rd annual conference on Computer graphics and interactive techniques*, 1996. 2

[21] Zhengqi Li, Simon Niklaus, Noah Snavely, and Oliver Wang. Neural scene flow fields for space-time view synthesis of dynamic scenes. In *CVPR*, 2021. 3

[22] David B Lindell, Julien NP Martel, and Gordon Wetzstein. Autoint: Automatic integration for fast neural volume rendering. In *CVPR*, 2021. 2, 3, 6, 7, 8, 11, 13

[23] Lingjie Liu, Jiatao Gu, Kyaw Zaw Lin, Tat-Seng Chua, and Christian Theobalt. Neural sparse voxel fields. In *NeurIPS*, 2020. 3, 6, 8

[24] Lingjie Liu, Marc Habermann, Viktor Rudnev, Kripasindhu Sarkar, Jiatao Gu, and Christian Theobalt. Neural actor: Neural free-view synthesis of human actors with pose control. *ACM Transactions on Graphics (TOG)*, 2021. 3

[25] Stephen Lombardi, Tomas Simon, Jason Saragih, Gabriel Schwartz, Andreas Lehrmann, and Yaser Sheikh. Neural volumes: Learning dynamic renderable volumes from images. In *SIGGRAPH*, 2019. 3

[26] Julien N. P. Martel, David B. Lindell, Connor Z. Lin, Eric R. Chan, Marco Monteiro, and Gordon Wetzstein. Acorn: Adaptive coordinate networks for neural scene representation. *ACM Transactions on Graphics (TOG)*, 40(4), 2021. 3, 8

[27] Ricardo Martin-Brualla, Noha Radwan, Mehdi SM Sajjadi, Jonathan T Barron, Alexey Dosovitskiy, and Daniel Duckworth. Nerf in the wild: Neural radiance fields for unconstrained photo collections. In *CVPR*, 2021. 3

[28] Lars Mescheder, Michael Oechsle, Michael Niemeyer, Sebastian Nowozin, and Andreas Geiger. Occupancy networks: Learning 3d reconstruction in function space. In *CVPR*, 2019. 3

[29] Ben Mildenhall, Pratul P Srinivasan, Rodrigo Ortiz-Cayon, Nima Khademi Kalantari, Ravi Ramamoorthi, Ren Ng, and Abhishek Kar. Local light field fusion: Practical view synthesis with prescriptive sampling guidelines. *ACM Transactions on Graphics (TOG)*, 38(4):1–14, 2019. 2, 3

[30] Ben Mildenhall, Pratul P Srinivasan, Matthew Tancik, Jonathan T Barron, Ravi Ramamoorthi, and Ren Ng. Nerf: Representing scenes as neural radiance fields for view synthesis. In *ECCV*, 2020. 1, 2, 3, 6, 7, 8, 11, 12, 13

[31] Thomas Neff, Pascal Stadlbauer, Mathias Parger, Andreas Kurz, Joerg H. Mueller, Chakravarty R. Alla Chaitanya, Anton Kaplanyan, and Markus Steinberger. Donerf: Towards

real-time rendering of compact neural radiance fields using depth oracle networks. *Comput. Graph. Forum*, 40(4):45–59, 2021. 2

[32] Michael Oechsle, Michael Niemeyer, Christian Reiser, Lars Mescheder, Thilo Strauss, and Andreas Geiger. Learning implicit surface light fields. In *International Conference on 3D Vision (3DV)*, 2020. 3

[33] Jeong Joon Park, Peter Florence, Julian Straub, Richard Newcombe, and Steven Lovegrove. Deepsdf: Learning continuous signed distance functions for shape representation. In *CVPR*, 2019. 3

[34] Keunhong Park, Utkarsh Sinha, Jonathan T Barron, Sofien Bouaziz, Dan B Goldman, Steven M Seitz, and Ricardo Martin-Brualla. Nerfies: Deformable neural radiance fields. In *ICCV*, 2021. 3, 6

[35] Sida Peng, Junting Dong, Qianqian Wang, Shangzhan Zhang, Qing Shuai, Xiaowei Zhou, and Hujun Bao. Animatable neural radiance fields for modeling dynamic human bodies. In *ICCV*, 2021. 3

[36] Eric Penner and Li Zhang. Soft 3d reconstruction for view synthesis. *ACM Transactions on Graphics (TOG)*, 36(6):1–11, 2017. 3

[37] Daniel Rebain, Wei Jiang, Soroosh Yazdani, Ke Li, Kwang Moo Yi, and Andrea Tagliasacchi. Derf: Decomposed radiance fields. In *CVPR*, 2021. 3

[38] Christian Reiser, Songyou Peng, Yiyi Liao, and Andreas Geiger. Kilonerf: Speeding up neural radiance fields with thousands of tiny mlps. In *ICCV*, 2021. 2, 3, 6

[39] Gernot Riegler and Vladlen Koltun. Free view synthesis. In *ECCV*, 2020. 3

[40] Gernot Riegler and Vladlen Koltun. Stable view synthesis. In *CVPR*, 2021. 3

[41] Darius Rückert, Linus Franke, and Marc Stamminger. Adop: Approximate differentiable one-pixel point rendering. *arXiv preprint arXiv:2110.06635*, 2021. 3

[42] Lixin Shi, Haitham Hassanieh, Abe Davis, Dina Katabi, and Fredo Durand. Light field reconstruction using sparsity in the continuous fourier domain. *ACM Transactions on Graphics (TOG)*, 34(1):1–13, 2014. 3

[43] Meng-Li Shih, Shih-Yang Su, Johannes Kopf, and Jia-Bin Huang. 3d photography using context-aware layered depth inpainting. In *CVPR*, 2020. 3

[44] Harry Shum and Sing Bing Kang. Review of image-based rendering techniques. In *Visual Communications and Image Processing 2000*, volume 4067, pages 2–13, 2000. 3

[45] Vincent Sitzmann, Julien Martel, Alexander Bergman, David Lindell, and Gordon Wetzstein. Implicit neural representations with periodic activation functions. In *NeurIPS*, 2020. 3

[46] Vincent Sitzmann, Semon Rezchikov, William T Freeman, Joshua B Tenenbaum, and Fredo Durand. Light field networks: Neural scene representations with single-evaluation rendering. In *NeurIPS*, 2021. 2, 3, 8

[47] Vincent Sitzmann, Justus Thies, Felix Heide, Matthias Nießner, Gordon Wetzstein, and Michael Zollhofer. Deepvoxels: Learning persistent 3d feature embeddings. In *CVPR*, 2019. 3

[48] Vincent Sitzmann, Michael Zollhöfer, and Gordon Wetzstein. Scene representation networks: Continuous 3d-structure-aware neural scene representations. In *NeurIPS*, 2019. 3

[49] Matthew Tancik, Pratul P Srinivasan, Ben Mildenhall, Sara Fridovich-Keil, Nithin Raghavan, Utkarsh Singhal, Ravi Ramamoorthi, Jonathan T Barron, and Ren Ng. Fourier features let networks learn high frequency functions in low dimensional domains. In *NeurIPS*, 2020. 4

[50] Ayush Tewari, Ohad Fried, Justus Thies, Vincent Sitzmann, Stephen Lombardi, Kalyan Sunkavalli, Ricardo Martin-Brualla, Tomas Simon, Jason Saragih, Matthias Nießner, et al. State of the art on neural rendering. *Computer Graphics Forum*, 39(2):701–727, 2020. 1, 3

[51] Ayush Tewari, Justus Thies, Ben Mildenhall, Pratul Srinivasan, Edgar Tretschk, Yifan Wang, Christoph Lassner, Vincent Sitzmann, Ricardo Martin-Brualla, Stephen Lombardi, Tomas Simon, Christian Theobalt, Matthias Niessner, Jonathan T. Barron, Gordon Wetzstein, Michael Zollhoefer, and Vladislav Golyanik. Advances in neural rendering, 2021. 1

[52] Edgar Tretschk, Ayush Tewari, Vladislav Golyanik, Michael Zollhofer, Christoph Lassner, and Christian Theobalt. Non-rigid neural radiance fields: Reconstruction and novel view synthesis of a dynamic scene from monocular video. In *ICCV*, 2021. 3

[53] Richard Tucker and Noah Snavely. Single-view view synthesis with multiplane images. In *CVPR*, 2020. 3

[54] Shubham Tulsiani, Richard Tucker, and Noah Snavely. Layer-structured 3d scene inference via view synthesis. In *ECCV*, 2018. 3

[55] Suren Vagharshakyan, Robert Bregovic, and Atanas Gotchev. Light field reconstruction using shearlet transform. *IEEE TPAMI*, 40(1):133–147, 2017. 3

[56] Bennett Wilburn, Neel Joshi, Vaibhav Vaish, Eino-Ville Talvala, Emilio R. Antúnez, Adam Barth, Andrew Adams, Mark Horowitz, and Marc Levoy. High performance imaging using large camera arrays. *ACM Trans. Graph.*, 24(3):765–776, 2005. 2, 6, 7, 11, 12, 13

[57] Suttisak Wizadwongsa, Pakkapon Phongthawee, Jiraphon Yenphraphai, and Supasorn Suwajanakorn. NeX: Real-time view synthesis with neural basis expansion. In *CVPR*, 2021. 3, 12

[58] Gaochang Wu, Yebin Liu, Qionghai Dai, and Tianyou Chai. Learning sheared epi structure for light field reconstruction. *IEEE TIP*, 28(7):3261–3273, 2019. 3

[59] Gaochang Wu, Mandan Zhao, Liangyong Wang, Qionghai Dai, Tianyou Chai, and Yebin Liu. Light field reconstruction using deep convolutional network on epi. In *CVPR*, 2017. 3

[60] Fanbo Xiang, Zexiang Xu, Milos Hasan, Yannick Hold-Geoffroy, Kalyan Sunkavalli, and Hao Su. Neutex: Neural texture mapping for volumetric neural rendering. In *CVPR*, 2021. 3

[61] Henry Wing Fung Yeung, Junhui Hou, Jie Chen, Yuk Ying Chung, and Xiaoming Chen. Fast light field reconstruction with deep coarse-to-fine modeling of spatial-angular clues. In *ECCV*, 2018. 3

[62] Alex Yu, Ruilong Li, Matthew Tancik, Hao Li, Ren Ng, and Angjoo Kanazawa. Plenoctrees for real-time rendering of neural radiance fields. In *CVPR*, 2021. 2, 3, 6

[63] Shuaifeng Zhi, Tristan Laidlow, Stefan Leutenegger, and Andrew Davison. In-place scene labelling and understanding with implicit scene representation. In *ICCV*, 2021. 3

[64] Tinghui Zhou, Richard Tucker, John Flynn, Graham Fyffe, and Noah Snavely. Stereo magnification: learning view synthesis using multiplane images. *ACM Transactions on Graphics (TOG)*, 2018. 3

A. Implementation Details

We include additional implementation details for our method for both the dense dataset (Stanford Light Field [56]) and sparse forward facing dataset (Real Forward-Facing [30]). We additionally include information about the NeRF [30] and AutoInt [22] baselines.

A.1. Stanford Light Field Dataset

Calibration information is not provided with the Stanford Light Field dataset, apart from the (x,y) positions of all images on the camera plane π^{xy}. All Stanford Light Fields images as provided are parameterized with respect to a plane π^{uv} that approximately cuts through the center of the scene. A pixel coordinate corresponds to a coordinate on this plane π^{uv}, rather than a plane at infinity. As such, we heuristically set the location of the π^{xy} to $z=-1$, and the location of the object plane to $z=0$. We scale the camera positions so that they lie between $[-0.25, 0.25]$ in both x and y, and the π^{uv} coordinates so they lie between $[-1,1]$. We take intersection coordinates with π^{xy} and π^{uv} as our initial ray parameterization.

For all scenes we set the near distance for NeRF to 0.5 and the far distance to 2, except for the Knights scene, where we set the near distance to 0.25. Note that, as defined, the scene coordinates may differ from the true (metric) world space coordinates by a projective ambiguity. However, multi-view constraints still hold (intersecting rays remain intersecting, epipolar lines remain epipolar lines), and thus NeRF is able to recover accurate reconstructions, despite this ambiguity.

A.2. Real Forward-Facing Dataset

For the Real Forward-Facing Dataset, we perform all experiments in NDC space. For our subdivided model, we re-parameterize each ray $\mathbf{r}$ within a voxel υ by first transforming space so that the voxel center lies at the origin. We then intersect the transformed ray with the voxel's front and back planes, and take the coordinates of these intersections, which lie within the range $[-\textit{voxel width}, +\textit{voxel width}]$ in all dimensions, as the parameterization.

A.3. NeRF and AutoInt Baselines

We train NeRF for 400k iterationss with a batch size of 1,024 for all scenes. We use the predictions of these trained NeRF models for teacher data for the Real Forward-Facing scenes.

AutoInt does not provide pretrained models and training with their reported parameters on a V100 GPU with 16GB of memory leads to out-of-memory errors. They also do not provide multi-GPU training code. As such, we report the quantitative metrics for their method and for NeRF published in their paper, which come from models trained at the same resolution (504×378), and using the same heldout views as ours on the Real Forward-Facing Dataset. We run our quantitative evaluation on a few of our trained NeRF models to verify that the numbers they report are similar to ours.

B. Importance of Light Field Parameterization

Here, we expand on the discussion in Section 4 of the main paper and describe why our light field parameterization is crucial for enabling good view interpolation. Let the two planes in the initial two plane parameterization be π^{xy} and π^{uv}, with local coordinates (x,y) and (u,v). In addition, let us denote the plane of the textured square as π^{st} with local coordinates (s,t), and assume that it is between π^{xy} and π^{uv}. Assume, without loss of generality, that the depth of π^{xy} is 0, and suppose the depths of π^{st} and π^{uv} are z_{st} and z_{uv} respectively.

For a ray originating at $(\hat{x},\hat{y})$ on π^{xy} and passing through $(\hat{s},\hat{t})$ on π^{st}, by similar triangles we can write:

$$\hat{s}-\hat{x} = (\hat{u}-\hat{x})\frac{z_{uv}}{z_{st}}, \tag{9}$$

$$\hat{t}-\hat{y} = (\hat{v}-\hat{y})\frac{z_{uv}}{z_{st}}, \tag{10}$$

which gives

$$\hat{u} = \frac{\hat{x}(z_{uv}-z_{st})+\hat{s}}{z_{uv}}, \tag{11}$$

$$\hat{v} = \frac{\hat{y}(z_{uv}-z_{st})+\hat{t}}{z_{uv}}. \tag{12}$$

Recall that the positional encoding of the 4D input parameterization $\gamma(\hat{x},\hat{y},\hat{u},\hat{v})$ will be fed into the light field network. Denoting two-vectors as complex numbers for convenience, and using Euler's formula $e^{i\theta} = \cos\theta + i\sin\theta$, the k-th positional encoding with frequency f_k can be written as:

$$\gamma(\hat{x},\hat{y},\hat{u},\hat{v}) = (e^{if_k\hat{x}}, e^{if_k\hat{y}}, e^{if_k\hat{u}}, e^{if_k\hat{v}}).$$

Thus:

$$\gamma(\hat{u}) = e^{i\frac{f_k}{z_{uv}}\hat{x}(z_{uv}-z_{st})}\cdot e^{i\frac{f_k}{z_{uv}}\hat{s}}, \tag{13}$$

$$\gamma(\hat{v}) = e^{i\frac{f_k}{z_{uv}}\hat{y}(z_{uv}-z_{st})}\cdot e^{i\frac{f_k}{z_{uv}}\hat{t}}. \tag{14}$$

For perfect interpolation, we would like the output of the light field network to only depend on $(\hat{s},\hat{t})$. We would also like to be able to express high-frequency details in $(\hat{s},\hat{t})$ using the light field network. We hypothesize that this entails recovering $(\gamma(\hat{s}),\gamma(\hat{t}))$ from $\gamma(\hat{x},\hat{y},\hat{u},\hat{v})$ internally within the light field MLP. As evidenced by the equation above, this would require *inferring* the factors $e^{i\frac{f_k}{z_{uv}}\hat{x}(z_{uv}-z_{st})}$ and $e^{i\frac{f_k}{z_{uv}}\hat{y}(z_{uv}-z_{st})}$ from $\gamma(\hat{u})$ and $\gamma(\hat{v})$.

In order to do this, we must sample $(\hat{x},\hat{y})$ at a rate of more than $\frac{2f_k(z_{uv}-z_{st})}{z_{uv}}$ *for every* $(\hat{u},\hat{v})$—i.e., the Nyquist rate. The greater the distance $(z_{uv}-z_{st})$, the larger the required sampling rate. For sampling rates lower than the Nyquist rate, it is in general not possible to uniquely recover these factors. We suspect that this leads to obviously incorrect reconstruction of EPIs for bad initial parameterizations (as evidenced in Figure 7 of the main text).

By learning a re-parameterization of the light field, such that π^{uv} is moved towards π^{st}, we can more easily recover $(\gamma(\hat{s}),\gamma(\hat{t}))$ with smaller sampling rates. In the extreme case, only one sample is required when $(z_{uv}-z_{st})=0$. As in the feature-embedding approach, the finite capacity of the light field MLP will drive the embedding network to learn to map rays intersecting the same point on the textured square to the same point in the latent space—and thus will drive learning of an optimal re-parameterization.

B.1. Empirical Validation

In order to support the above claims, we perform a set of simple experiments with parameterization. In particular, we choose the *Amethyst* scene from the Stanford Light Field dataset [56], which has very little depth variation. As described in Section A.1, each Stanford light field has the object plane π^{st} at $z=0$. We re-parameterize the input light field for π^{uv} at $z=0,1,3$, train our model *without* an embedding network, and report validation metrics, as well as showing reconstructed epipolar images. See Figure B.1 and Table B.1.

As hypothesized, the models trained with the object plane closer to $z=0$ perform better qualitatively and quantitatively. While this is, perhaps, an obvious result, we believe that it is an important one. In particular, it means that light fields with worse initial parameterization (where worse means farther distance of π^{uv} from the dominant object plane π^{st}), must be sampled at a higher rate in order to be reconstructed well *with an architecture that uses positional encoding* [30]. We believe that similar analyses will hold for non-planar scenes, as well as scenes exhibiting view dependence (with perhaps non-planar level sets).

C. More Experimental Results

We show per-scene metrics in Tables C.1 and C.2. Additionally, we highly encourage readers to visit our project webpage, which contains image comparisons for every scene, video comparisons for a select few scenes, and brief qualitative comparisons to NeX [57] on scenes from its Shiny dataset.

Table B.1. **Empirical validation of parameterization.** We calculate PSNR, SSIM, and LPIPS for our model without embedding trained on different initial parameterizations.

π^{uv} location	PSNR↑	SSIM↑	LPIPS↓
$z=0$	**29.631**	**0.937**	**0.059**
$z=1$	<u>24.411</u>	<u>0.848</u>	<u>0.096</u>
$z=3$	21.491	0.790	0.146

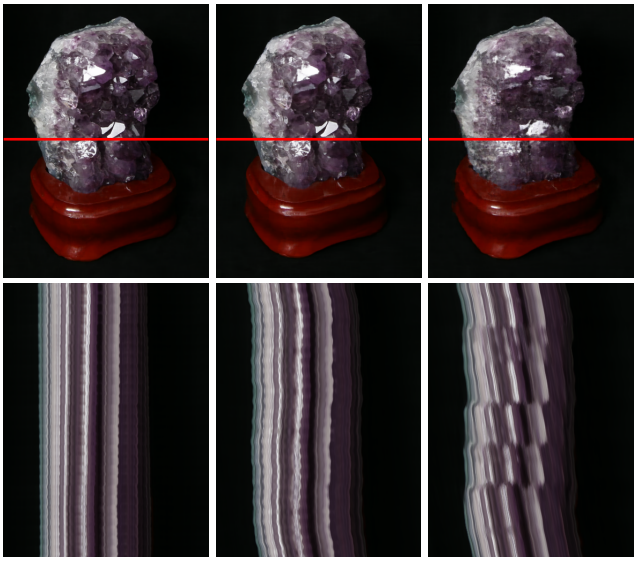

$z=0$ $z=1$ $z=3$

Figure B.1. **Effect of initial parameterization.** The *top* row shows predicted images, *bottom* predicted EPIs. Reconstruction becomes progressively worse for a worse initial parameterization (π^{uv} moving further and further from the object plane at $z=0$).

Table C.1. Per-scene breakdown results from NeRF's Real Forward-Facing dataset [30].

Scene	PSNR↑				SSIM↑				LPIPS↓			
	NeRF [30]	AutoInt [22]	Ours	Ours (w/ t)	NeRF [30]	AutoInt [22]	Ours	Ours (w/ t)	NeRF [30]	AutoInt [22]	Ours	Ours (w/ t)
Fern	**26.92**	23.51	24.25	26.06	**0.903**	0.810	0.850	0.893	**0.085**	0.277	0.114	0.104
Flower	28.57	28.11	28.71	**28.90**	0.931	0.917	**0.934**	**0.934**	0.057	0.075	**0.038**	0.053
Fortress	**32.94**	28.95	31.46	32.60	**0.962**	0.910	0.954	0.961	**0.024**	0.107	0.027	0.028
Horns	29.26	27.64	**30.12**	29.76	0.947	0.908	**0.955**	0.952	0.058	0.177	**0.044**	0.062
Leaves	**22.50**	20.84	21.82	22.27	0.851	0.795	0.847	**0.855**	0.103	0.156	**0.086**	0.104
Orchids	**21.37**	17.30	20.29	21.10	**0.800**	0.583	0.766	0.794	0.108	0.302	**0.103**	0.113
Room	33.60	30.72	33.57	**34.04**	0.980	0.966	0.979	**0.981**	0.038	0.075	**0.037**	**0.037**
T-rex	28.26	27.18	**29.41**	28.80	0.953	0.931	**0.959**	**0.959**	0.049	0.080	**0.034**	0.040

Table C.2. Per-scene breakdown results from the Stanford Light Field dataset [56].

Scene	PSNR↑			SSIM↑			LPIPS↓		
	NeRF [30]	X-Fields [2]	Ours	NeRF [30]	X-Fields [2]	Ours	NeRF [30]	X-Fields [2]	Ours
Amethyst	39.746	37.232	**40.120**	0.984	0.982	**0.985**	0.026	0.032	**0.019**
Beans	**42.519**	40.911	41.659	**0.9944**	0.9931	0.9933	0.014	0.017	**0.012**
Bracelet	36.461	34.112	**36.586**	0.9909	0.9857	**0.9913**	0.0094	0.0260	**0.0087**
Bulldozer	38.968	37.350	**39.389**	0.983	0.986	**0.987**	0.063	0.032	**0.024**
Bunny	43.370	42.251	**43.591**	0.9892	0.9894	**0.9900**	0.029	0.022	**0.013**
Chess	**41.146**	37.996	40.910	0.9915	0.9882	**0.9920**	0.028	0.034	**0.016**
Flowers	37.910	37.590	**39.951**	0.977	0.981	**0.984**	0.076	0.035	**0.030**
Knights	**35.978**	31.491	34.591	**0.986**	0.974	0.982	**0.0142**	0.0501	0.0143
Tarot (Small)	34.221	30.830	**36.046**	0.982	0.975	**0.989**	0.014	0.033	**0.006**
Tarot (Large)	**24.907**	24.154	24.904	0.910	0.893	**0.914**	0.059	0.074	**0.039**
Treasure	34.761	33.904	**37.465**	0.972	0.977	**0.982**	0.027	0.041	**0.019**
Truck	40.723	38.883	**41.440**	0.986	0.986	**0.989**	0.087	0.042	**0.033**